

Effect of uniaxial strain on the excitonic properties of monolayer C₃N: A symmetry-based analysisMatteo Zanfagnini ^{1,2,*}, Nicola Spallanzani ², Miki Bonacci ^{1,2}, Elisa Molinari ^{1,2}, Alice Ruini ^{1,2}, Marilia J. Caldas ³,
Andrea Ferretti ² and Daniele Varsano ²¹*Dipartimento di Scienze Fisiche, Informatiche, e Matematiche, Università di Modena e Reggio Emilia, I-41125 Modena, Italy*²*Centro S3, CNR-Istituto Nanoscienze, I-41125 Modena, Italy*³*Instituto de Física, Universidade de São Paulo, Cidade Universitária, 05508-900 São Paulo, Brazil*

(Received 29 October 2022; revised 23 December 2022; accepted 5 January 2023; published 30 January 2023)

In recent years, the application of mechanical stress has become a widespread experimental method to tune the electronic and optical properties of two-dimensional (2D) materials. In this work, we investigate the impact of uniaxial tensile strain along zigzag and armchair directions on the excitonic properties of graphene-like C₃N, a single-layer indirect-gap material with relevant mechanical and optical properties. To do that, we develop a tight-binding Bethe-Salpeter equation framework based on a Wannier-function description of the frontier bands of the system, and use it to compute both dark and bright excitons of C₃N for different applied strain configurations. Then, we use this model approach to classify excitons of pristine and strained C₃N according to the crystal symmetry and to explain the appearance of bright excitons with intense optical anisotropy in strained C₃N, even at small strains. Finally, the effect of strain on the exciton dispersion at small center-of-mass momenta is discussed, with special focus on the implications for 2D linear-nonanalytic dispersions.

DOI: [10.1103/PhysRevB.107.045430](https://doi.org/10.1103/PhysRevB.107.045430)**I. INTRODUCTION**

Since its experimental realization [1,2], monolayer C₃N (ML-C₃N) has been intensively studied from a theoretical point of view, to fully characterize its electronic [3], optical [4,5], mechanical [6–8], and electrochemical properties [9–13]. Among the interesting features of ML-C₃N, we focus here on its optical and mechanical response. As ML-C₃N is a 2D material, the combination of electron confinement and enhanced electron-hole interaction (due to reduced electronic screening) gives rise to strong excitonic effects, which characterize its optical response [4,5]. At the same time, DFT and molecular dynamics calculations [6] have predicted the capability of ML-C₃N to sustain strong uniaxial strains, up to about 10%, without failure.

Motivated by recent advances in the experimental application of relatively intense mechanical stresses to 2D materials [14–16], in this work we discuss how the excitonic properties of ML-C₃N are modified by external uniaxial strain, when applied along high-symmetry directions, such as zigzag and armchair (see Fig. 1). As fully *ab initio* calculations of excitonic effects are computationally very demanding, especially for 2D materials, here we develop a simpler approach to solve the Bethe-Salpeter equation (BSE) [17–19] and apply it to the case of ML-C₃N subject to different strain conditions.

As discussed in the following sections, this model describes the single-particle states involved in the lowest-lying excitons through a tight-binding (TB) Hamiltonian and approximates the electron-hole interaction using quantities derived from *ab initio* calculations [3,20–22].

Based on this model, we discuss the appearance of excitons in strained C₃N with strong optical anisotropy, and we have provided a rationale for this behavior through group theory arguments. Further, taking advantage of the computational simplicity of the model, we have analyzed the small-momentum excitonic dispersion, both in pristine and strained C₃N, revealing the effect of uniaxial strain on the small-momentum linear nonanalytic dispersion.

Our results show that the presence of a few percent strain is already able to induce a strong anisotropy in the exciton dispersion close to Γ regarding the direction of applied strain, and furthermore leading to anisotropic brightening of some of the low-lying excitons.

The article is organized as follows: In Secs. II and III, we describe the approach used to solve the BSE and check the validity of the adopted approximations, by comparing our results for pristine ML-C₃N with those computed fully *ab initio*. In Sec. IV we discuss how the bright excitons in unstrained C₃N are modified by the applied strain, while in Sec. V we present a similar analysis for the lowest dark excitons in pristine C₃N. Finally, in Sec. VI we consider the effect of strain on the exciton dispersion computed for small center-of-mass momenta.

II. METHODS

In this section we present the method used throughout this work to study the excitonic properties of pristine and strained ML-C₃N. As previous works [3–5] have shown that the valence and conduction states involved in the formation of the lowest-lying excitons have π character, we have modeled these bands through a TB Hamiltonian [23] focusing on the $2p_z$ orbitals, once we define the xy plane as the monolayer

*Corresponding author: matteo.zanfagnini@unimore.it

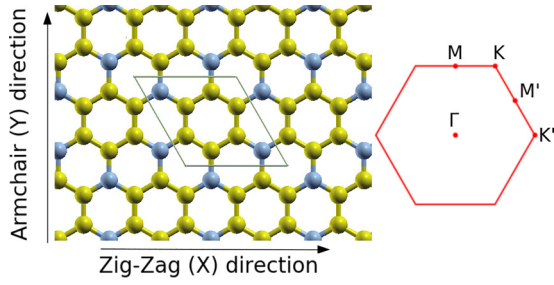


FIG. 1. Left: Crystal structure of C_3N , where yellow (light-blue) spheres represent carbon (nitrogen) atoms. High-symmetry armchair and zigzag directions where strain is applied are also highlighted. Right: Hexagonal Brillouin zone of pristine C_3N , with the high-symmetry points considered in this work.

plane:

$$H_{\alpha\beta}(\mathbf{k}) = \sum_{\mathbf{R}} e^{i\mathbf{k}\cdot\mathbf{R}} \langle \alpha 0 | \hat{H} | \beta \mathbf{R} \rangle. \quad (1)$$

In Eq. (1), \mathbf{R} is a lattice vector, \mathbf{k} is a point sampling the 2D Brillouin zone (BZ), and $t(\alpha 0; \beta \mathbf{R}) = \langle \alpha 0 | \hat{H} | \beta \mathbf{R} \rangle$ corresponds to the hopping between a $2p_z$ orbital localized on atom α in the unit cell at $\mathbf{R} = 0$ and a $2p_z$ orbital localized on atom β in the unit cell at \mathbf{R} . The hopping parameters have been evaluated fully *ab initio* adopting the following procedure: For each strain configuration, we have computed single-particle electronic states and energies at the DFT level (with GGA-PBE [24] approximation for the exchange-correlation kernel) using the plane-wave Quantum ESPRESSO [25,26] package. Then, we have extracted maximally localized Wannier functions (MLWFs) [23,27] with the Wannier90 code [28–30], making use of the band disentanglement method [31]. As expected, the obtained MLWFs exhibit a $2p_z$ -like character, as shown in Fig. 2. Finally, the hopping parameters appearing in Eq. (1) have been obtained as the Hamiltonian matrix elements on the computed MLWF basis. Details about DFT calculations and Wannierization procedure are provided in the Supplemental Material [32] (SM) (see also Refs. [33–36] therein).

The diagonalization of $H_{\alpha\beta}(\mathbf{k})$ gives access to single-particle energies and states: More precisely, we have solved the eigenvalue problem

$$\sum_{\beta} H_{\alpha\beta}(\mathbf{k}) c_{\beta}(n\mathbf{k}) = \epsilon_{n\mathbf{k}} c_{\alpha}(n\mathbf{k}) \quad (2)$$

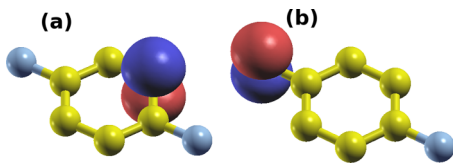


FIG. 2. Example of maximally localized Wannier functions localized on carbon (a) and nitrogen atoms (b). The obtained Wannier functions exhibit a $2p_z$ -like character, with comparable spatial spreads.

obtaining $\epsilon_{n\mathbf{k}}$ (the energy of the n th band at point \mathbf{k}) and $c_{\alpha}(n\mathbf{k})$, the projection of Bloch state $|n\mathbf{k}\rangle$ on the MLWF α , i.e.,

$$|\psi_{n\mathbf{k}}\rangle = \frac{1}{\sqrt{N_c}} \sum_{\alpha} c_{\alpha}(n\mathbf{k}) \sum_{\mathbf{R}} e^{i\mathbf{k}\cdot\mathbf{R}} |\alpha \mathbf{R}\rangle, \quad (3)$$

$|\alpha \mathbf{R}\rangle$ being the $2p_z$ -like MLWF localized at $\tau_{\alpha} + \mathbf{R}$, with τ_{α} corresponding to the atomic site of atom α in the unit cell. We notice here that the quantities $\epsilon_{n\mathbf{k}}$ provide an accurate description of the single-particle energies obtained at the DFT level, as the hopping parameters were computed by Wannierizing DFT bands. In this work we include the effect of quasiparticle corrections using a scissor/stretching operator, as in Ref. [5]. To reduce the computational complexity, in the following we use the scissor/stretching parameters computed in the pristine case for all the considered strain perturbations, assuming a negligible dependence of the quasiparticle corrections on the relatively small strain discussed in this work. The BSE is solved within the resonant Tamm-Dancoff approximation [18,19]; i.e., we compute exciton energies and wave functions by diagonalizing the Hermitian excitonic Hamiltonian:

$$H_{\mathbf{Q}}(v\mathbf{k}; v'c'\mathbf{k}') = (\epsilon_{c,\mathbf{k}+\mathbf{Q}} - \epsilon_{v\mathbf{k}}) \delta_{c,c'} \delta_{v,v'} \delta_{\mathbf{k},\mathbf{k}'} + K_{\mathbf{Q}}^d(v\mathbf{k}; v'c'\mathbf{k}') + K_{\mathbf{Q}}^x(v\mathbf{k}; v'c'\mathbf{k}'), \quad (4)$$

where $K_{\mathbf{Q}}^d$ and $K_{\mathbf{Q}}^x$ are the direct and the exchange kernels [18,19], respectively, and v, v' (c, c') the band indexes for the valence (conduction) states included in the BSE. In the following, we will always include the last occupied valence and the two lowest unoccupied conduction bands in the construction of the BSE kernel, as the lowest-energy excitons in ML- C_3N mainly involve transitions among those states. \mathbf{Q} represents the planar center-of-mass momentum of the excitons. In the calculations presented in this work, we have used a $121 \times 121 \times 1$ Monkhorst-Pack [37] grid to sample the BZ, which guarantees exciton energies converged within 1 meV.

We now provide the expressions of the direct and exchange kernels, obtained starting from our TB description of the single-particle states, while a detailed derivation of $K_{\mathbf{Q}}^d(v\mathbf{k}; v'c'\mathbf{k}')$ and $K_{\mathbf{Q}}^x(v\mathbf{k}; v'c'\mathbf{k}')$ is presented in the Supplemental Material [32]. First, in order to simplify the notation, we introduce the auxiliary quantities

$$\rho_{\mathbf{p}+\mathbf{G}}(n\mathbf{k}; m\mathbf{k}') = \sum_{\alpha} e^{-i\tau_{\alpha}\cdot(\mathbf{p}+\mathbf{G})} c_{\alpha}(n\mathbf{k}) c_{\alpha}^*(m\mathbf{k}'), \quad (5)$$

where $\mathbf{p} = \mathbf{k} - \mathbf{k}'$, the index α runs over the MLWF in the unit cell, and τ_{α} identifies the position of the corresponding center. Then, for the direct and exchange terms in the BSE kernel, we obtain:

$$K_{\mathbf{Q}}^d(v\mathbf{c}\mathbf{k}; v'\mathbf{c}'\mathbf{k}') = -\frac{1}{4\pi^2} \sum_{\mathbf{G}} v_{2D}(\mathbf{q} + \mathbf{G}) |F(\mathbf{q} + \mathbf{G})|^2 I_d(\mathbf{q} + \mathbf{G}) [\rho_{\mathbf{q}+\mathbf{G}}^*(c, \mathbf{k} + \mathbf{Q}; c', \mathbf{k}' + \mathbf{Q}) \rho_{\mathbf{q}+\mathbf{G}}(v\mathbf{k}; v'\mathbf{k}')], \quad (6)$$

$$K_{\mathbf{Q}}^x(v\mathbf{c}\mathbf{k}; v'\mathbf{c}'\mathbf{k}') = \frac{2}{4\pi^2} \sum_{\mathbf{G}} v_{2D}(\mathbf{q} + \mathbf{G}) |F(\mathbf{Q} + \mathbf{G})|^2 X_{ex}(\mathbf{Q} + \mathbf{G}) [\rho_{\mathbf{Q}+\mathbf{G}}^*(c, \mathbf{k} + \mathbf{Q}; v\mathbf{k}) \rho_{\mathbf{Q}+\mathbf{G}}(c', \mathbf{k}' + \mathbf{Q}; v'\mathbf{k}')], \quad (7)$$

where v_{2D} is the 2D Coulomb potential, $\mathbf{q} = \mathbf{k} - \mathbf{k}'$, and the factor 2 in the exchange term indicates that we are only considering singlet excitons. In the above expressions, F , I_d , and X_{ex} are functions explicitly defined below in Eqs. (11)–(13).

We now briefly summarize the approximations used to obtain the direct and exchange kernels, as given by Eqs. (6) and (7). First, we adopt a cylindrical approximation for the $2p_z$ -like Wannier functions $w(\mathbf{r} - \mathbf{R} - \tau_\alpha)$, i.e.,

$$w(\mathbf{r} - \mathbf{R} - \tau_\alpha) \approx f_\alpha(\mathbf{r}_\parallel - \mathbf{R} - \tau_\alpha) h_\alpha(z) \text{sgn}(z), \quad (8)$$

decoupling the in-plane components \mathbf{r}_\parallel of the position vector \mathbf{r} from the out-of-plane component z [38]. The functions f_α and h_α were obtained using the definitions

$$\begin{aligned} f_\alpha(\mathbf{r}_\parallel - \mathbf{R} - \tau_\alpha) &= A_\alpha^f \int_{-\infty}^{+\infty} dz |w(\mathbf{r} - \mathbf{R} - \tau_\alpha)| \\ &= A_\alpha^f e^{-B_\alpha |\mathbf{r}_\parallel - \mathbf{R} - \tau_\alpha|} [1 + B_\alpha |\mathbf{r}_\parallel - \mathbf{R} - \tau_\alpha|] \end{aligned} \quad (9)$$

and

$$\begin{aligned} h_\alpha(z) &= A_\alpha^h \int dr_\parallel |w(\mathbf{r} - \mathbf{R} - \tau_\alpha)| \\ &= A_\alpha^h [|z| e^{-B_\alpha |z|} (1 + B_\alpha |z|)], \end{aligned} \quad (10)$$

where A_α^f and A_α^h are normalization constants.

In practice, f_α is the average of the modulus of a $2p_z$ orbital along z at fixed planar coordinate $\mathbf{r}_\parallel - \mathbf{R} - \tau_\alpha$, while h_α is its plane average, for each z . Finally, B_α is a parameter related to the spread of the MLWF, which depends on the atomic site τ_α where the Wannier function is localized. As the spatial spread obtained *ab initio* for N and C localized MLWF are very close, with differences smaller than 10%, we have chosen B_α as the average of the functions B obtained for the different Wannier functions, so that the functional form of h and f does not explicitly depend on the atom on which they are centered. Using these definitions, we can write the expression of the functions F , I_d , and X_{ex} appearing in the direct and exchange kernels, Eqs. (6) and (7), as

$$F(\mathbf{q} + \mathbf{G}) = \int d\mathbf{r}_\parallel |f(\mathbf{r}_\parallel)|^2 e^{i(\mathbf{q}+\mathbf{G}) \cdot \mathbf{r}_\parallel}, \quad (11)$$

$$\begin{aligned} I_d(\mathbf{q} + \mathbf{G}) &= \int dz dz' dz_1 e^{-|\mathbf{q}+\mathbf{G}| \cdot |z_1 - z'|} \\ &\quad \times |h(z)|^2 \epsilon_{\mathbf{q}+\mathbf{G}}^{-1}(z, z_1) |h(z')|^2, \end{aligned} \quad (12)$$

$$\begin{aligned} X_{ex}(\mathbf{Q} + \mathbf{G}) &= \int dz dz' e^{-|\mathbf{Q}+\mathbf{G}| \cdot |z - z'|} \\ &\quad \times |h(z)|^2 |h(z')|^2, \end{aligned} \quad (13)$$

with \mathbf{G} a vector of the 2D reciprocal lattice.

The function X_{ex} has been computed by direct numerical integration, using the analytical expression of h , while I_d ,

which can be interpreted as an effective screening for the 2D Coulomb potential v_{2D} , requires the knowledge of the static inverse dielectric function ϵ^{-1} . The function ϵ^{-1} has been computed within random phase approximation (RPA) using the Yambo code [39,40], in the case of unstrained monolayer, and then used to construct the function I_d as outlined in the Supplemental Material [32], starting from Eq. (12). As we have assumed the effect of small strains on the electronic screening to be negligible, we use the I_d computed for the unstrained monolayer for all the strain configurations considered in this work. Furthermore, we remark that in order to obtain the expression of I_d given in Eq. (12) we neglect the in-plane local field effects; i.e., we choose

$$\epsilon^{-1}(\mathbf{q} + \mathbf{G}, \mathbf{G}_z; \mathbf{q} + \mathbf{G}', \mathbf{G}'_z) \approx \delta_{\mathbf{G}, \mathbf{G}'} \epsilon^{-1}(\mathbf{q} + \mathbf{G}; \mathbf{G}_z, \mathbf{G}'_z),$$

being \mathbf{G} and \mathbf{G}_z the in-plane and out-of-plane components of a reciprocal lattice vector. Instead, the nonlocality with respect to z of the inverse dielectric function ϵ^{-1} has been fully taken into account, since it is fundamental to obtain a proper description of electronic screening in 2D materials [20,41].

The computational advantage of our method is twofold: First, the use of a TB model for single-particle states permits an accurate mapping of single-particle states and energies on small matrices, with dimension equal to the number of used Wannier functions, from which electronic states and energies can be obtained by simple diagonalizations at all \mathbf{k} points in the BZ. Second, modeling the dielectric screening through the function I_d permits obtaining electron-electron interaction on very fine grids, without explicit calculations for all scattering \mathbf{q} vectors. We point out that the presented approach can be extended to other 2D systems, by defining proper approximations for the obtained atomic Wannier functions, in the calculations of the functions I_d and F .

Finally, the absorption spectra of pristine and strained C_3N have been evaluated computing the imaginary part of the dielectric function defined as

$$\varepsilon(\omega) = 1 - \frac{8\pi}{V} \sum_{\lambda} \frac{D_{\lambda}}{\omega - E_{\lambda} + i\eta}, \quad (14)$$

where V is the unit cell volume, λ is an index running over excitons with null momentum \mathbf{Q} , and D_{λ} is the oscillator strength (OS) of the exciton λ , given by

$$D_{\lambda} = \lim_{\mathbf{Q} \rightarrow 0} \frac{1}{|\mathbf{Q}|^2} \left| \sum_{v\mathbf{c}\mathbf{k}} \langle v\mathbf{k} | e^{-i\mathbf{Q} \cdot \mathbf{r}} | c\mathbf{k} \rangle A_{\lambda}(v\mathbf{k}; c\mathbf{k}) \right|^2, \quad (15)$$

where $A_{\lambda}(v\mathbf{k}; c\mathbf{k})$ is the envelope function of exciton λ , and $\mathbf{Q} = |Q| \hat{j}$. Notice that D_{λ} depends on the polarization direction, as the limit in Eq. (15) is performed by letting the momentum \mathbf{Q} go to zero along the direction \hat{j} , which is chosen as the in-plane polarization direction of the incoming light.

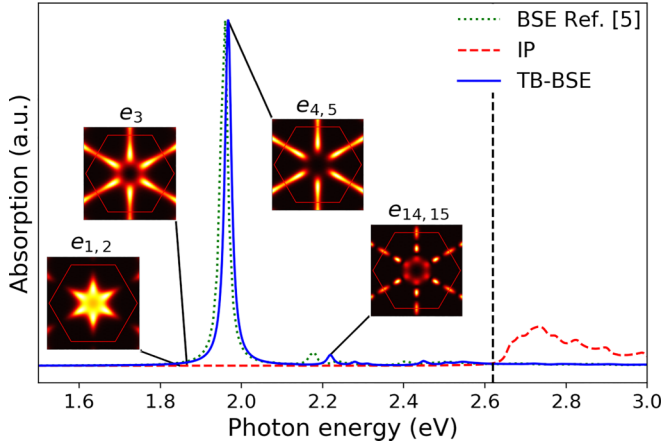


FIG. 3. Absorption spectrum of monolayer C_3N computed with the model described in Sec. II. The continuous blue line (dashed red line) represents the spectrum computed with (without, independent particle IP) the electron-hole interaction in the BSE kernel. The green dotted line is the fully *ab initio* BSE spectrum obtained in Ref. [5], while the vertical dashed black line indicates the position of the quasiparticle direct band gap corresponding to the onset of independent particle (IP) absorption. These spectra were computed assuming light polarization along the zigzag direction, and analogous results were found for different polarizations. \mathbf{k} -resolved contributions to the exciton wave functions are shown for the first five lowest energy excitons, and for the resonances responsible for the higher-energy absorption peak at about 2.2 eV. All the spectra have been convoluted with a Lorentzian broadening of 10 meV. The labels e_i indicate the excitation energies in ascending order.

III. MODEL VALIDATION

We now test the validity of the approximations discussed in the preceding section, by comparing the *ab initio* results recently obtained [5] for $\mathbf{Q} = 0$ excitons in unstrained ML- C_3N with those obtained by the TB-BSE approach here presented. In Fig. 3 we show the absorption spectrum computed with and without the electron-hole interaction in the BSE kernel (continuous blue line and dashed red line, respectively), together with fully *ab initio* BSE results of Ref. [5] shown as a dotted green line. In agreement with previous results [4,5], we find an optical spectrum dominated by a single intense peak which corresponds to a pair of degenerate excitons, $e_{4,5}$, exhibiting a large binding energy, of about 0.6 eV. These excitons are mainly due to valence-conduction transitions located along the ΓM directions, as visualized by considering the \mathbf{k} -resolved contributions to the exciton wave functions:

$$A(\mathbf{k}) = \sum_{vc} \sum_{\lambda} |A_{\lambda}(v\mathbf{k}; c\mathbf{k})|^2, \quad (16)$$

where the summation over the exciton index λ is present only for degenerate excitons and $A_{\lambda}(v\mathbf{k}; c\mathbf{k})$ is the exciton envelope function, whose square modulus indicates the weight of the single-particle transition $(v, \mathbf{k}) \rightarrow (c, \mathbf{k})$ to exciton λ . These functions are shown for the lowest resonances in the insets of Fig. 3.

A second structure at a higher energy of 2.219 eV appears in the optical spectrum, due to a pair of degenerate excitons

TABLE I. Comparison between *ab initio* BSE and TB-BSE excitation energies of the first five lowest excitons.

Method	$e_{1,2}$	e_3	$e_{4,5}$
<i>Ab initio</i> BSE [5]	1.821	1.854	1.957
Model TB-BSE	1.848	1.866	1.967

$e_{14,15}$. This structure is also present in the *ab initio* absorption spectrum, at a slightly smaller energy (2.18 eV). This exciton pair will not be further discussed in the following. At energies below the $e_{4,5}$ intense peak, we also find three dark excitations, i.e., a pair of degenerate excitons $e_{1,2}$ and a single resonance e_3 .

To quantify more precisely the comparison between the model and the *ab initio* results, in Table I we collect the excitation energies of the first five excitons in monolayer C_3N computed with *ab initio* methods and with the TB-BSE approach. We note that the model reproduces with high accuracy the *ab initio* results, with a small blueshift of exciton energies, which is anyhow smaller than 40 meV.

Having validated the TB-BSE model, we now turn our attention to the effect of mechanical strain on these five lowest excitonic resonances, dividing them according to their optical activity in the unstrained monolayer. In particular, in Sec. IV we discuss the behavior of bright excitons $e_{4,5}$, while in Sec. V we consider the dark excitons $e_{1,2}$ and e_3 .

IV. EFFECT OF STRAIN ON BRIGHT EXCITONS

We now consider in detail the effect of uniaxial strain on the pair of bright excitons $e_{4,5}$, responsible for the intense absorption peak in pristine C_3N . In Fig. 4 we plot the absorption spectra for zigzag [panel (a)] and armchair [panel (b)] strains, with strengths in the range 0%–3.5%. We consider the polarization along both the zigzag (continuous red lines) and armchair (dashed blue lines) directions. We point out that, within our choice of the reference system, the zigzag direction X coincides with the Cartesian direction x while the armchair axis Y corresponds to the direction y in the monolayer plane (see Fig. 1).

The effect of strain is twofold: First, the double degeneracy observed in pristine C_3N is removed, with the appearance of two excitations whose splitting increases linearly with strain, at a rate of about $6.0 \frac{\text{meV}}{\%}$ for both strain directions. Second, these two resonances exhibit a strong optical anisotropy: In the case of zigzag strain the lowest-energy exciton (here called e_4) is bright for light polarization along x , while it is dark if the incoming electric field is oriented along the y direction. Differently, the highest-energy exciton e_5 can only absorb photons with polarization along the armchair direction. This strain-induced optical anisotropy, also proposed in Ref. [42] within a single-particle description of C_3N optical properties, is therefore also present once excitonic effects are included. The situation is exactly the opposite in the case of armchair strain, where e_4 (e_5) becomes dark for incoming light polarization along the zigzag (armchair) direction.

The observed strain-induced optical anisotropy is further highlighted by computing the oscillator strengths D_4 and D_5

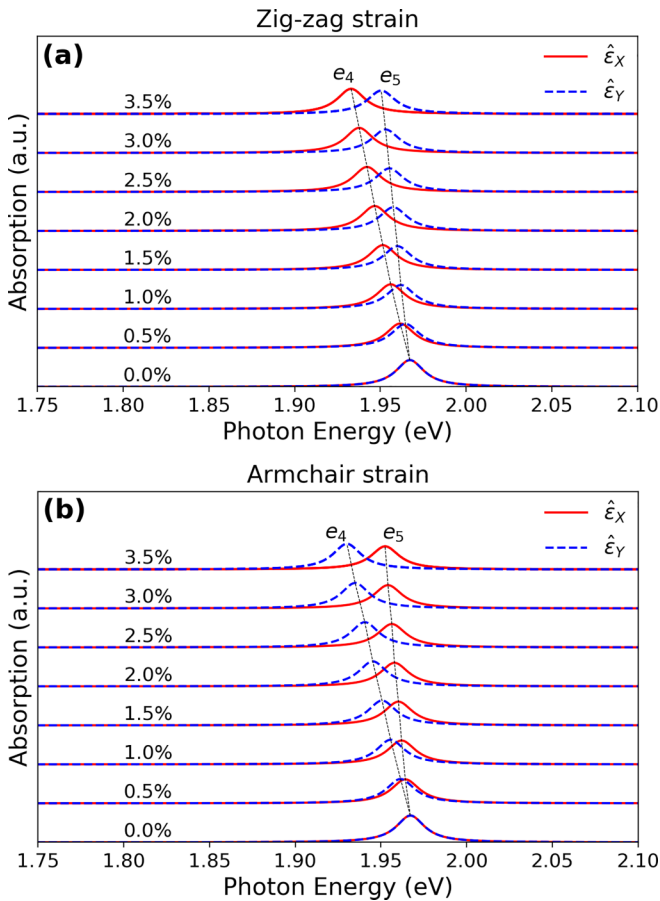


FIG. 4. (a) Absorption spectra of ML-C₃N under uniaxial strain along the zigzag direction: Continuous red lines correspond to light polarized along the zigzag (X) direction, while dashed blue lines to light polarized along the armchair (Y) direction. Spectra for different values of applied strain are rigidly shifted vertically to make the plot more readable. The black dashed lines highlight the splitting of the twofold degenerate exciton $e_{4,5}$ in pristine C₃N into two separate excitons, here called e_4 and e_5 . All the spectra are convoluted with a Lorentzian broadening of 10 meV. (b) Same as (a), for externally applied strain along the armchair direction.

as a function of the polarization angle with respect to the zigzag direction. This is shown in Fig. 5, where we consider a strain of 2.0% for both cases. We see that with zigzag strain these two excitons have an oscillator strength characterized by a two-lobed angular pattern, with e_4 having a nodal line along the y direction and e_5 along the x direction. Analogously, in the case of armchair strain the OS patterns have similar features, but the profiles for the two split excitons are exchanged. We remark that the observed optical anisotropy does not depend on the value of the applied strain, as, also for larger strains, the nodal lines at which the OS becomes zero are always present: As shown in the Supplemental Material [32], for a larger strain of 3.0% the polar plots have similar properties.

To properly characterize the excitons e_4 and e_5 we computed the corresponding transition distribution functions $A(\mathbf{k})$, as defined in Eq. (16). These are shown in Fig. 6 in the case of a 2.0% strain along both the zigzag and armchair

directions (we checked that the following considerations are valid independently of the value of the applied strain within the considered range). In the case of zigzag strain, the exciton e_4 is mainly due to transitions along the ΓM direction, while e_5 is characterized by a wave function $A(\mathbf{k})$ peaked for \mathbf{k} along $\Gamma M'$ direction. On the other hand, in the case of armchair strain, the function $A(\mathbf{k})$ for the lowest-energy exciton e_4 is nonzero along $\Gamma M'$, while for e_5 is mainly localized along the ΓM direction.

The reason why in zigzag strained ML-C₃N the lowest exciton is mainly confined along ΓM , while in the case of armchair strain it becomes localized along $\Gamma M'$, can be understood by considering the effect of strain on the electronic band structure. In Fig. 7 we present the electronic bands computed at the DFT-PBE level for zigzag (a) and armchair (b) strain, both equal to 2.0%, compared to pristine C₃N, represented by solid black lines. Considering the DFT bands, we see that one of the main effects of uniaxial strain (in both directions) is to induce different electronic band dispersions along the ΓM and the $\Gamma M'$ directions, otherwise equivalent by symmetry in the pristine case.

The connection with the excitonic transition distribution becomes clearer by looking at Figs. 7(c) and 7(d) where we report the difference $\epsilon_c(\mathbf{k}) - \epsilon_v(\mathbf{k})$ for the last occupied valence band v and the first unoccupied conduction band c along the path $M-\Gamma-M'$ in the BZ. We see that in zigzag strained C₃N the lowest transition energies $\epsilon_c(\mathbf{k}) - \epsilon_v(\mathbf{k})$ occur along ΓM . Therefore, the exciton involving transitions along this direction (i.e., e_4) has a smaller excitation energy than the exciton e_5 , mainly composed by single-particle transitions along $\Gamma M'$. Analogously, by looking at Fig. 7(d), we can see that for armchair strain the minimum of $\epsilon_c(\mathbf{k}) - \epsilon_v(\mathbf{k})$ falls along $\Gamma M'$ so that we effectively expect the lowest-energy exciton to be mainly composed by transitions along this direction. We point out that the relative energy differences among the directions ΓM and $\Gamma M'$ could be affected by the addition of quasiparticle effects, but the dispersions along the two directions are expected to remain different as a result of the symmetry breaking effect of applied uniaxial strain. Furthermore, this strain induced change of the electronic bands along ΓM and $\Gamma M'$ directions can also justify the observed increasing of the splitting among excitons e_4 and e_5 as a function of strain. Considering the case of zigzag strain, by increasing strain we observe that the difference between the minima of $\epsilon_c(\mathbf{k}) - \epsilon_v(\mathbf{k})$ computed for \mathbf{k} along ΓM and $\Gamma M'$ progressively increases: As the exciton e_4 is mainly composed by v - c transitions along ΓM while e_5 is localized along $\Gamma M'$ their energy splitting will increase as a consequence of the increased energy splitting among the single-particle states involved in the two excitons. Similar reasoning can be done in case of armchair strain.

Symmetry analysis

Having described how the main absorption peak in pristine C₃N is modified by the application of strain, we now classify the two resulting excitons e_4 and e_5 in terms of their symmetry properties, starting from the symmetry characterization of excitons in pristine C₃N and then focusing our attention on the strained monolayer. The point group of pristine C₃N

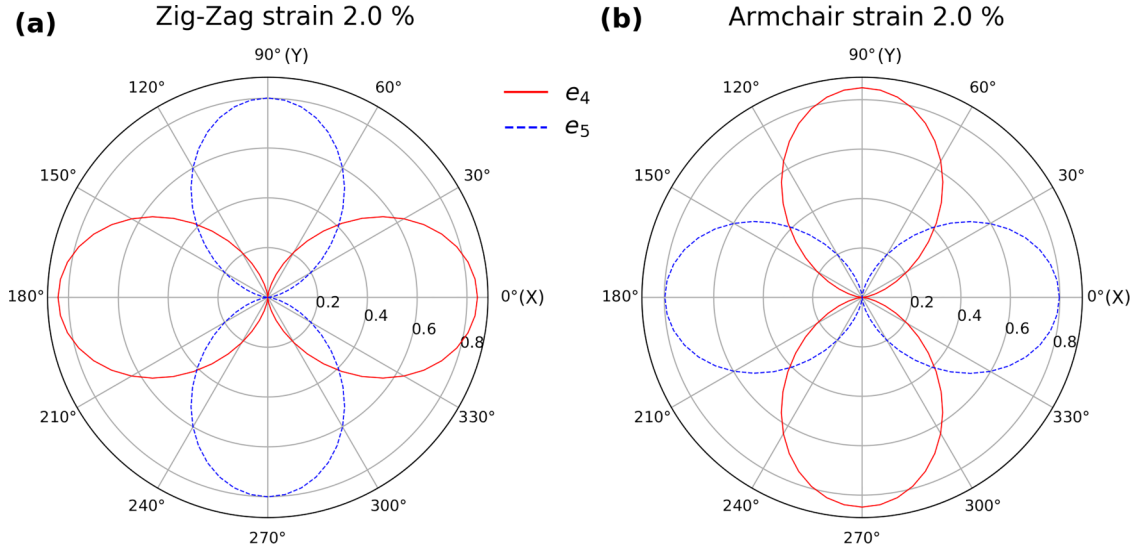


FIG. 5. Polar plot of the oscillator strengths D_λ defined in Eq. (15) for excitons e_4 and e_5 , in the case of zigzag strain (a) and armchair strain (b) of 2.0%, as a function of the in-plane light polarization direction, measured starting from the zigzag (X) axis. Concentric lines represent isovalues for the modulus of the exciton oscillator strength $|D_\lambda|$.

is D_{6h} , which contains the in-plane symmetries of a hexagon combined with the mirror symmetry operation σ_h with respect to the monolayer plane. Within our approach, we describe the electronic properties (and therefore the excitonic ones) of the system with an effective tight-binding model, which is purely planar. Therefore, analogously to the work of Galvani *et al.* [43], in the following we classify excitons considering only the in-plane symmetry operations contained in the point group D_{6h} , which form the subgroup C_{6v} . Once strain is applied to ML- C_3N , the symmetry of the system is lowered and the full point group becomes D_{2h} . Following the reasoning just outlined, we will then classify excitons according to the

irreducible representations of the subgroup C_{2v} , only composed by in-plane symmetries.

We start by discussing the degenerate excitons $e_{4,5}$ of pristine C_3N . In order to understand which is the irreducible representation of C_{6v} which transforms as these excitons, for each symmetry operator \hat{S} representing a class of C_{6v} we have computed the character:

$$\chi[\hat{S}] = \sum_{\lambda=\{e_{4,5}\}} \langle \lambda | \hat{S} | \lambda \rangle, \quad (17)$$

where the sum over λ runs on the two degenerate excitons $e_{4,5}$. This quantity is the trace of the symmetry operator \hat{S} on the 2D space spanned by these excitons and its evaluation is described in Appendix A.

Our calculations give the characters summarized in Table II. From these results, we can associate the doublet $e_{4,5}$ to the irreducible representation E_1 of C_{6v} , consistently with their bright nature. In fact, an exciton λ is bright only if the matrix element $\langle 0 | \hat{\mathbf{D}} | \lambda \rangle$ is nonzero, being $|0\rangle$ the excitonic vacuum, $\hat{\mathbf{D}}$ the exciton dipole operator (here assumed as constrained in the ML plane). The operator $\hat{\mathbf{D}}$ behaves like an in-plane vector, which, in turns, transforms as the E_1 irreducible representation of C_{6v} , while the excitonic vacuum belongs to the fully symmetric representation A_1 . Therefore, the matrix element $\langle 0 | \hat{\mathbf{D}} | \lambda \rangle$ will be different from zero only for the excitons transforming according to irreducible representations Γ of C_{6v}

TABLE II. Characters χ , evaluated for each class of symmetry operations of the point group C_{6v} , considering the bright degenerate excitons $e_{4,5}$ of pristine ML- C_3N . Direct comparison with character table of C_{6v} indicates that this excitonic doublet transforms as the representation E_1 .

	E	$2C_6$	$2C_3$	C_2	$3\sigma_v$	$3\sigma_d$
χ	2	1	-1	-2	0	0

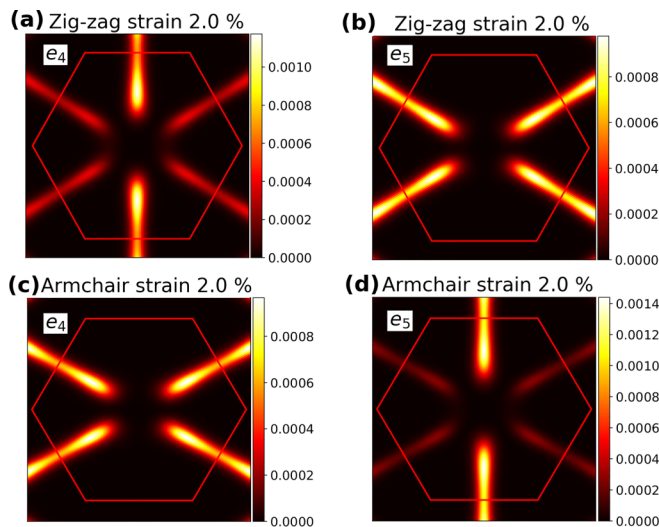


FIG. 6. Functions $A(\mathbf{k})$ defined in Eq. (16), computed for exciton e_4 (a) and e_5 (b) in the case of zigzag strain of 2.0%. (c) and (d) correspond to the same quantities shown in (a) and (b), but evaluated for ML- C_3N strained along the armchair direction.

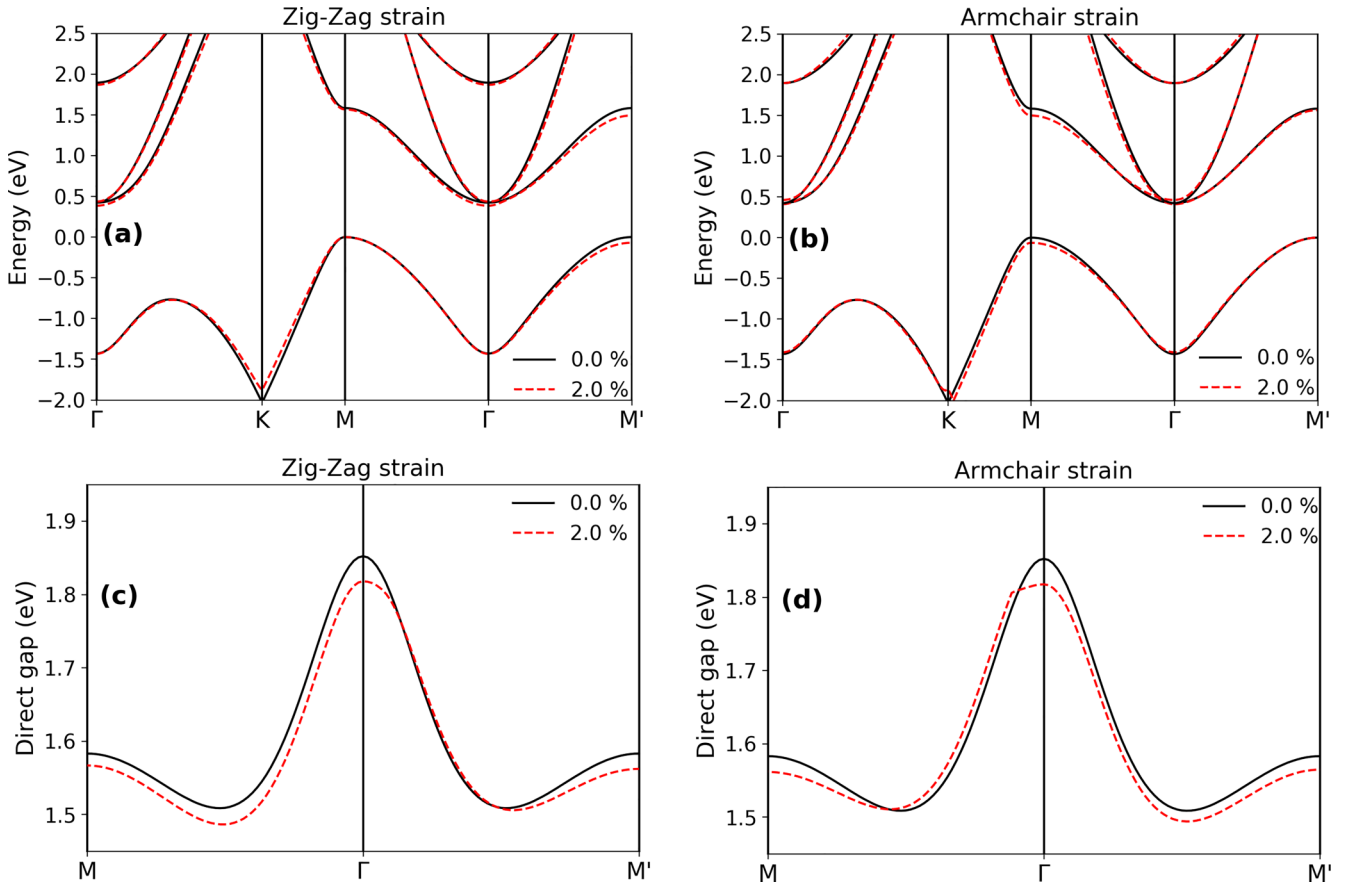


FIG. 7. (a) DFT-PBE band structure of ML-C₃N in the pristine case (solid black lines) and with a zigzag strain of 2.0% (dashed red lines); (b) same as (a), but for a 2.0% strain along the armchair direction. (c) Energy difference $\epsilon_c(\mathbf{k}) - \epsilon_v(\mathbf{k})$ between the lowest unoccupied conduction c and the highest occupied valence v for \mathbf{k} along the path M - Γ - M' for the unstrained case and for a 2.0% zigzag strain; (d) same as (c) for an armchair strain.

such that the direct product $E_1 \otimes \Gamma$ contains the representation A_1 . Straightforward application of group theory rules [44] for the direct product between irreducible representations of the same group indicates that the only representation satisfying this constraint is E_1 , in agreement with our numerical results summarized in Table II.

Considering the presence of uniaxial strain, the pair of excitons $e_{4,5}$ transforming as E_1 in unstrained C₃N will now be split into two excitons as there are no irreducible representations with dimension larger than 1 in C_{2v} , in agreement with our numerical findings. In order to classify these two excitons, we can apply the “great orthogonality theorem” of group theory [44] to decompose the E_1 representation of C_{6v} into irreducible representations of C_{2v} : Each representation of C_{2v} contained in E_1 then corresponds to each exciton e_4 and e_5 , as obtained in the presence of strain. Using the character tables of the C_{2v} group, we obtain $E_1(C_{6v}) = B_1(C_{2v}) \oplus B_2(C_{2v})$.

We now associate exciton e_4 and e_5 to the irreducible representations B_1 and B_2 . In order to do this, we could compute the characters for each exciton as discussed before for the degenerate pair $e_{4,5}$ in pristine C₃N. Instead, in this case we use a simpler approach, which consists in studying the wave function of these excitons in real space. Therefore,

we compute the quantity $\Psi_\lambda^{\alpha,\beta}(\mathbf{R})$ defined as

$$\Psi_\lambda^{\alpha,\beta}(\mathbf{R}) = \langle \mathbf{r}_h = \tau_\alpha; \mathbf{r}_e = \tau_\beta + \mathbf{R} | \lambda \rangle, \quad (18)$$

i.e., the probability amplitude to find, for the exciton λ , the electron localized in the $2p_z$ state on atom β in the unit cell \mathbf{R} and the hole on the orbital $2p_z$ on atom α in the cell at $\mathbf{R} = \mathbf{0}$. The detailed procedure for its evaluation within the TB-BSE formalism is reported in Appendix B.

In Fig. 8 we show the excitonic wave function for the states e_4 and e_5 in the presence of a uniaxial strain of 2.0% applied along the zigzag [(a), (b)] and armchair [(c), (d)] directions. In all cases, we assume the position of the hole to be fixed on a carbon atom denoted by the black dot and located on the symmetry plane σ_{yz} (represented by the dashed black line). Further, this function is generally complex valued: in this case we have properly chosen its global phase so that it assumes real values for all $\tau_\beta + \mathbf{R}$ [positive values red dots, negative values blue dots, diameter of a circle proportional to the modulus $|\Psi_\lambda^{\alpha,\beta}(\mathbf{R})|$]. With zigzag strain, the lowest exciton e_4 turns out to be odd with respect to the mirror reflection σ_{yz} , while the exciton e_5 is even: As $B_1(C_{2v})$ is odd and $B_2(C_{2v})$ is even under σ_{yz} operation, we can therefore assign e_4 to B_1 and e_5 to B_2 in the case of zigzag strain. Notice that these

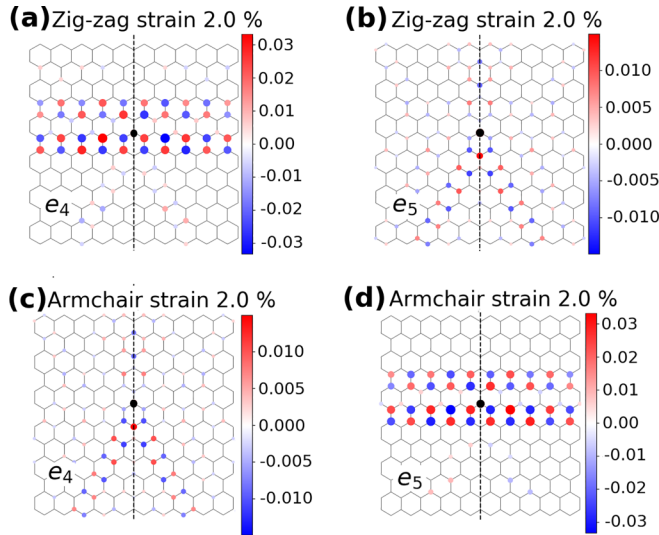


FIG. 8. Excitonic wave functions $\Psi_{\lambda}^{\alpha,\beta}(\mathbf{R})$, as defined in Eq. (18), computed respectively for the excitons e_4 (left) and e_5 (right), assuming a 2.0% strain along the zigzag direction (top) and the armchair direction (bottom). In all cases, we assume the hole to be fixed on the carbon atom marked by the black dot and positioned on the vertical dashed line, which represents the symmetry $y = 0$ axis.

assignments were further checked by computing the action of the symmetry operations of C_{2v} on these excitons, as outlined in Appendix A. The situation is exactly the opposite in the case of armchair strain, where the lowest exciton e_4 is even under σ_{yz} while the exciton e_5 is odd, so that they can be respectively assigned to B_2 and B_1 irreducible representations of C_{2v} .

The evaluation of $\Psi_{\lambda}^{\alpha,\beta}(\mathbf{R})$ at fixed hole position is useful to properly understand the symmetry properties of e_4 and e_5 , but it also underlines the strong spatial localization of the bright excitons in ML- C_3N under strain: This is especially apparent in the case of B_1 excitons [see Figs. 8(a) and 8(d)], where, once the hole is fixed along the y axis, the electron is constrained in an effective one-dimensional stripe of the material, even for relatively small applied strains.

We complete this analysis on bright excitons in strained C_3N by pointing out the symmetry-breaking origin of the optical anisotropy observed in absorption spectra obtained by numerical solution of the BSE. We have just seen that for any applied strain (along the zigzag or the armchair directions) the E_1 exciton of pristine ML- C_3N splits into two excitons transforming as the B_1 and B_2 irreducible representations of C_{2v} . Using group theory rules, we can verify that

$$\begin{aligned} \langle 0|D_x|B_1\rangle &\neq 0, & \langle 0|D_y|B_1\rangle &= 0, \\ \langle 0|D_x|B_2\rangle &= 0, & \langle 0|D_y|B_2\rangle &\neq 0, \end{aligned}$$

where D_x and D_y are the components along the x (zigzag) and the y (armchair) axes. These selection rules are a direct consequence of the fact that D_x (D_y) transforms as the B_1 (B_2) irreducible representation of C_{2v} . Therefore, we have strong optical anisotropy in strained C_3N monolayer, with one exciton becoming dark for the light polarization direction at which the other exhibits its highest OS, simply because of the

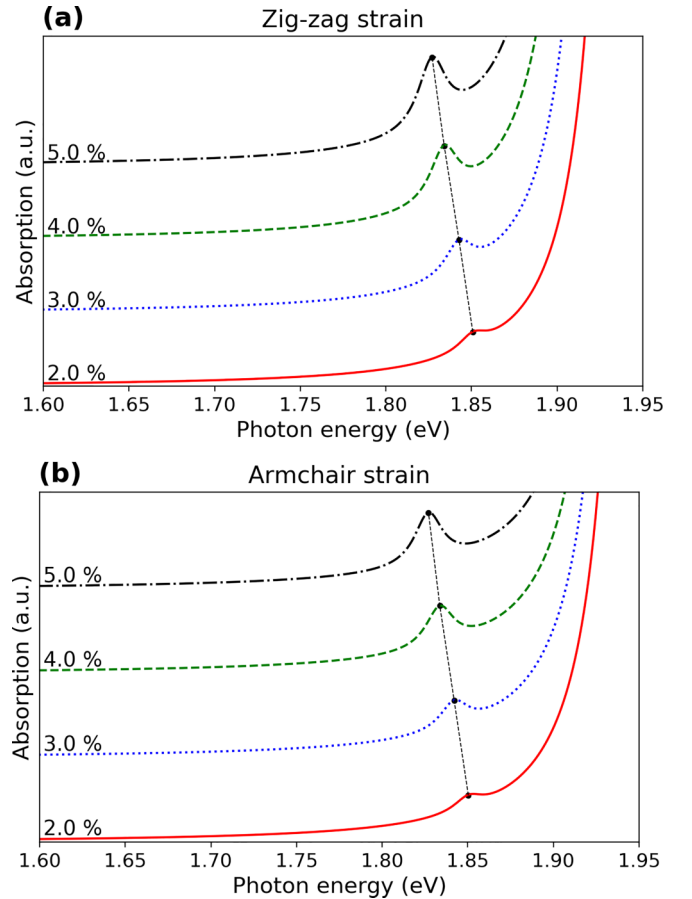


FIG. 9. (a) Low-energy tail of the absorption spectrum in ML- C_3N under uniaxial strain along zigzag direction. (b) Same as (a), but considering an externally applied strain along the armchair direction. All the spectra were convoluted with a Lorentzian broadening of 10 meV. Curves corresponding to different strain values are rigidly shifted vertically to make the plot more readable.

symmetry-lowering effect induced by the strain. Thus, while the strength of the applied strain does not control this linear dichroism, it tunes the energy splitting between these two excitons.

V. EFFECT OF STRAIN ON DARK EXCITONS

We now discuss the effect of strain on the lowest-lying dark excitons in pristine ML- C_3N , denoted as $e_{1,2}$ and e_3 in Fig. 3. By a direct inspection of Fig. 4, one can realize that these excitons should remain dark or acquire a negligible OS in the presence of strain, as the spectra are dominated by excitons e_4 and e_5 . To better clarify their optical behavior, in Fig. 9 we present the absorption spectrum at photon energies slightly smaller than the energy of excitons e_4 and e_5 for different strains. In particular, Fig. 9(a) corresponds to zigzag strains, Fig. 9(b) to armchair strains, while light polarization is kept fixed along the zigzag direction in both cases. We note that the rapidly increasing signal for higher energies corresponds to the contribution of excitons e_4 and e_5 already discussed in the previous section.

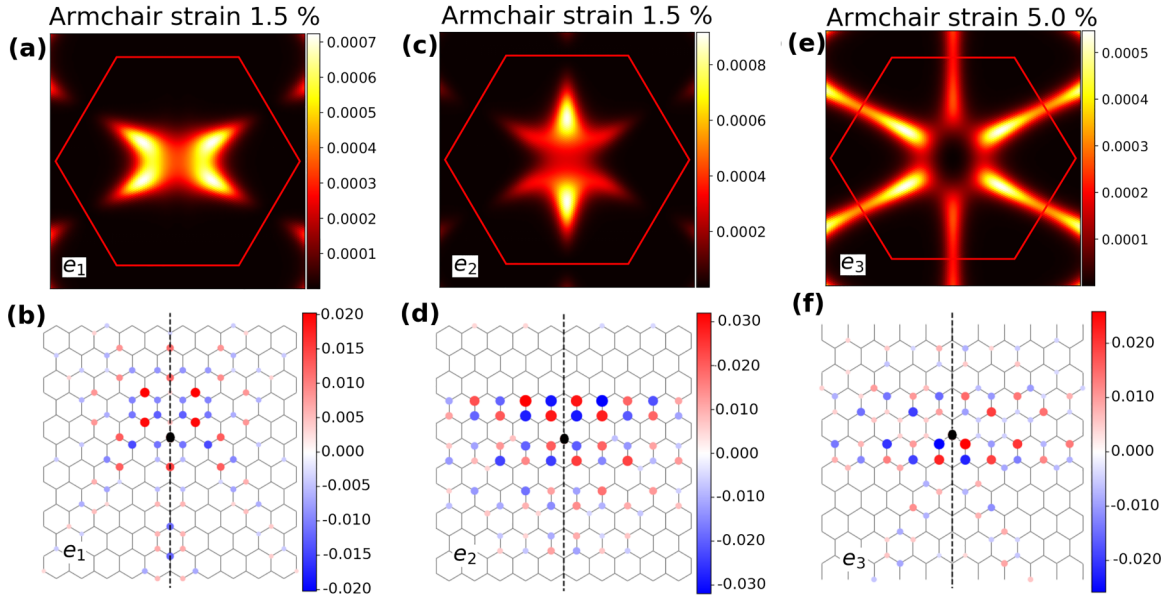


FIG. 10. Functions $A(\mathbf{k})$ for excitons e_1 , e_2 , and e_3 are shown in panels (a), (c), and (e); the applied strain is fixed to 1.5% (5.0%) in the case of excitons e_1 and e_2 (e_3), and it is always assumed along the armchair direction. Real-space representations $\Psi^{\alpha,\beta}(\mathbf{R})$ for the excitons e_1 , e_2 , and e_3 are displayed in panels (b), (d), and (f), computed for the same set of strain configurations.

For both strain directions, we notice the presence of a weak absorption feature in the tail of the main peak (not shown in Fig. 9), whose intensity progressively increases as a function of the applied strain. However, we point out that in the range of the considered strains (which are realistic values that can be efficiently applied to 2D materials experimentally) such an absorption peak is about two orders of magnitude smaller than the most intense absorption structure observed in Fig. 3 (see Supplemental Material [32] for a comparison of the relative intensities in the case of 4.0% zigzag strain). Such a feature comes from the dark exciton e_3 of pristine ML- C_3N , which acquires a small OS under the application of strain. Differently, the pair of degenerate excitons $e_{1,2}$ splits into two excitons e_1 and e_2 which remain dark even in the presence of strain.

We start our analysis of low-lying dark excitons focusing on the states coming from the degenerate pair $e_{1,2}$ in pristine ML- C_3N . Their \mathbf{k} -space $A(\mathbf{k})$ and real-space $\Psi_{\lambda}^{\alpha,\beta}(\mathbf{R})$ representations are given in Figs. 10(a)–10(d), in the case of armchair strain equal to 1.5%. Similarly to Sec. IV, we discuss these excitons starting from the symmetry properties of the degenerate pair $e_{1,2}$ in unstrained C_3N , from which they derive. Applying the approach discussed in Appendix A, we find that the pair $e_{1,2}$ transforms as the irreducible representation E_2 of the point group C_{6v} . Since the only excitons in pristine C_3N which have a nonzero OS for in-plane polarization are those transforming according to E_1 , excitons $e_{1,2}$ are dark by symmetry.

Uniaxial strain reduces the crystal point group from C_{6v} to C_{2v} ; therefore $E_2(C_{6v})$ is now a reducible representation of C_{2v} , which contains only the irreducible representations A_1 and A_2 of C_{2v} , i.e., $E_2(C_{6v}) = A_1(C_{2v}) \oplus A_2(C_{2v})$. As a consequence, the two split excitons e_1 and e_2 will transform as $A_1(C_{2v})$ and $A_2(C_{2v})$. This identification explains why these two excitons remain dark even in the strained crystal: Considering that D_x and D_y respectively transform as the

irreducible representations B_1 and B_2 of C_{2v} , all the possible direct products $B_i \otimes A_j$, with $i, j = \{1, 2\}$, do not contain the full symmetry representation A_1 of C_{2v} , so that the exciton dipole matrix element $\langle 0|\mathbf{D}|\lambda\rangle$ is always zero.

As before, we can exploit the real-space representation $\Psi^{\alpha,\beta}(\mathbf{R})$, as shown for example in Figs. 10(b) and 10(d), to assign $e_{1,2}$ to the irreducible representations $A_{1,2}$. Looking at Figs. 10(b) and 10(d), in the case of armchair strain, the lowest exciton e_1 is even under the σ_{yz} mirror reflection, while e_2 is odd. Looking at the character table for C_{2v} , we can therefore assign e_1 to A_1 and e_2 to A_2 . The same reasoning can be followed in the case of zigzag strain: The only difference is that in this case, the exciton e_1 (e_2) transforms as the irreducible representation A_2 (A_1) of the point group C_{2v} .

We now discuss the properties of exciton e_3 and justify in terms of group theory arguments the reason why it acquires a finite OS in strained C_3N . In the discussion we focus on the 5.0% strain case, though we note that the following comments remain qualitatively valid also for smaller strains. Looking at Fig. 10(e), we notice that the effect of strain along the armchair direction is to create an unbalance between the intensity of the \mathbf{k} -space wave function $A(\mathbf{k})$ along the ΓM and $\Gamma M'$ directions (as those are no longer equivalent in the presence of strain; see also Fig. 3 for comparison with the pristine case). The application of the symmetry operators of the C_{6v} point group on the exciton wave function e_3 in unstrained C_3N enables us to assign it to the irreducible representation B_1 of C_{6v} , which is dark for planar polarization of the incoming light, in good agreement with the absorption spectrum shown in Fig. 3. Interestingly, B_1 of C_{6v} corresponds to B_1 of C_{2v} : In fact, by looking at Fig. 10(f), we see that the real-space exciton wave function for e_3 is odd with respect to the mirror reflection about the yz plane, which is effectively the same behavior of $B_1(C_{2v})$ under σ_{yz} . As already discussed in the previous section, excitons transforming as $B_1(C_{2v})$ can have a

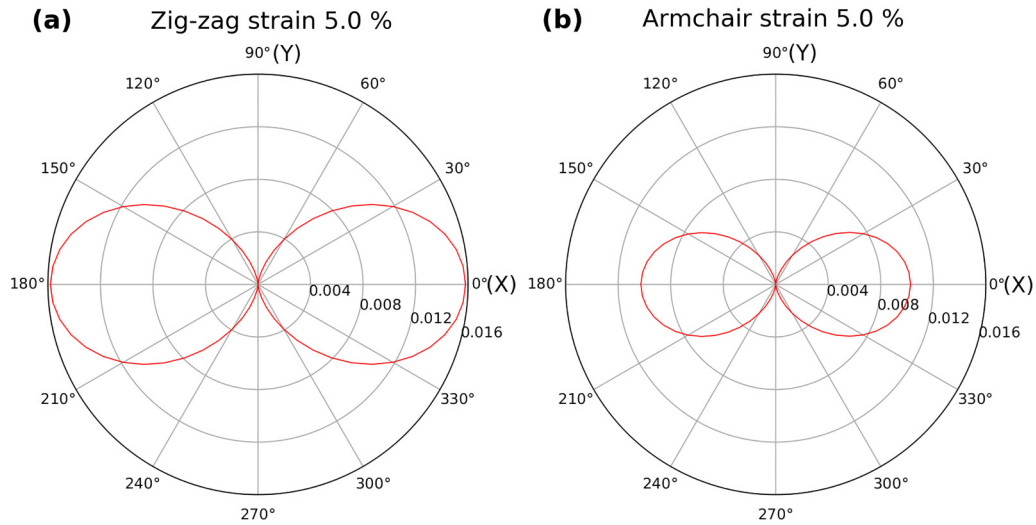


FIG. 11. Oscillator strength D_λ , defined in Eq. (15), computed for exciton e_3 as a function of the light polarization direction (measured with respect to the zigzag x axis), in the case of zigzag (a) and armchair (b) strain equal to 5.0%. The circles in both figures represent isovalues for the modulus of the exciton oscillator strength $|D_\lambda|$.

nonzero oscillator strength for light polarized along the zigzag direction. This justifies the appearance of a peak in the zigzag polarized absorption spectrum of strained ML- C_3N due to the e_3 exciton.

To further confirm the agreement between the numerical results and the proposed symmetry analysis, in Fig. 11 we display the profile of the oscillator strength associated to the exciton e_3 as a function of the polarization direction under a zigzag (a) and armchair (b) strain of 5.0%. We notice that, independently of the direction of the applied strain, the e_3 exciton has an anisotropic OS, showing a nodal line along the armchair direction y . This is due to the fact that it transforms as B_1 of C_{2v} for both the considered uniaxial strains, and, since $\langle 0|D_y|B_1\rangle$ is zero by symmetry, such an exciton cannot absorb light polarized along y . This is confirmed by numerical results, which also indicate that the OS associated to exciton e_3 becomes more intense (of almost a factor 2) when strain is applied along the zigzag rather than along the armchair axis.

VI. EXCITON DISPERSION AT SMALL MOMENTA

Up to now, we have discussed how excitons with null center-of-mass momentum \mathbf{Q} are modified via the application of tensile uniaxial strain. In this section, we focus on the dispersion of exciton energies as a function of finite momentum \mathbf{Q} [45]. A fully *ab initio* calculation of exciton band structure along high-symmetry directions in the BZ for pristine C_3N has been already presented in a previous work [5]. Here, by taking advantage of the TB-BSE approach developed in Sec. II, we deepen that analysis by computing the excitonic dispersion in both pristine and strained C_3N at small momenta \mathbf{Q} . The evaluation of small- \mathbf{Q} dispersions is very demanding (though possible [46]) within a fully *ab initio* approach, because of the limited \mathbf{Q} -points sampling accessible in practice. In this respect, in the present work we exploit the simplicity of our TB-BSE model to compute such a dispersion, which is known to strongly influence exciton dynamics and lifetimes [47,48].

In the following, we evaluate the lowest excitonic bands $E_\lambda(\mathbf{Q})$, taking \mathbf{Q} along the ΓM and $\Gamma K'$ directions, with intensity constrained to be smaller than $|\Gamma M|/5$ and $|\Gamma K'|/10$ in the two cases, respectively. In Fig. 12, we show the excitonic dispersion in the case of pristine ML- C_3N . Concerning the low-energy excitonic bands, departing from the dark excitons at Γ , we notice that the bands branching out of the E_2 doublet (excitons $e_{1,2}$) are characterized by a negative concavity, while the band starting from the exciton B_1 (e_3) presents positive concavity, as also found by *ab initio* calculations [5].

The most striking feature of the obtained band structure (not seen in the *ab initio* dispersion) is represented by the two bands which originate from the E_1 excitons at Γ ($e_{4,5}$), highlighted in Fig. 12 by red dots. We notice the presence of an almost flat band with negative concavity and of a

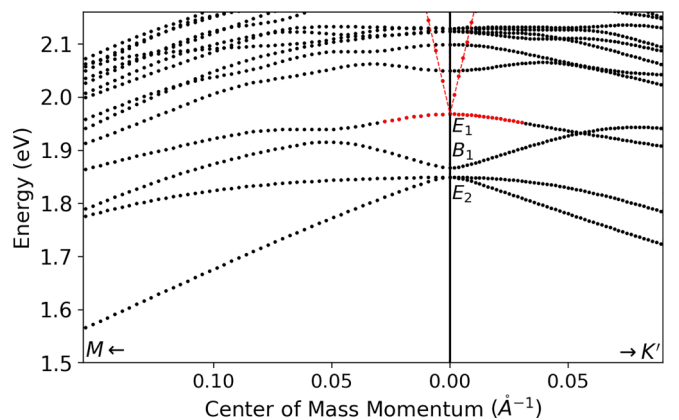


FIG. 12. Exciton dispersion in pristine C_3N for \mathbf{Q} in proximity of Γ and along the path $M-\Gamma-K'$. Red dots denote the excitonic bands departing from the bright excitons at Γ , transforming as E_1 ; the linear band dispersion of the highest band is also highlighted by dashed red lines, representing the obtained linear fits along the two high-symmetry directions. For completeness, $|\Gamma M| = 0.746 \text{\AA}^{-1}$ while $|\Gamma K'| = 0.861 \text{\AA}^{-1}$.

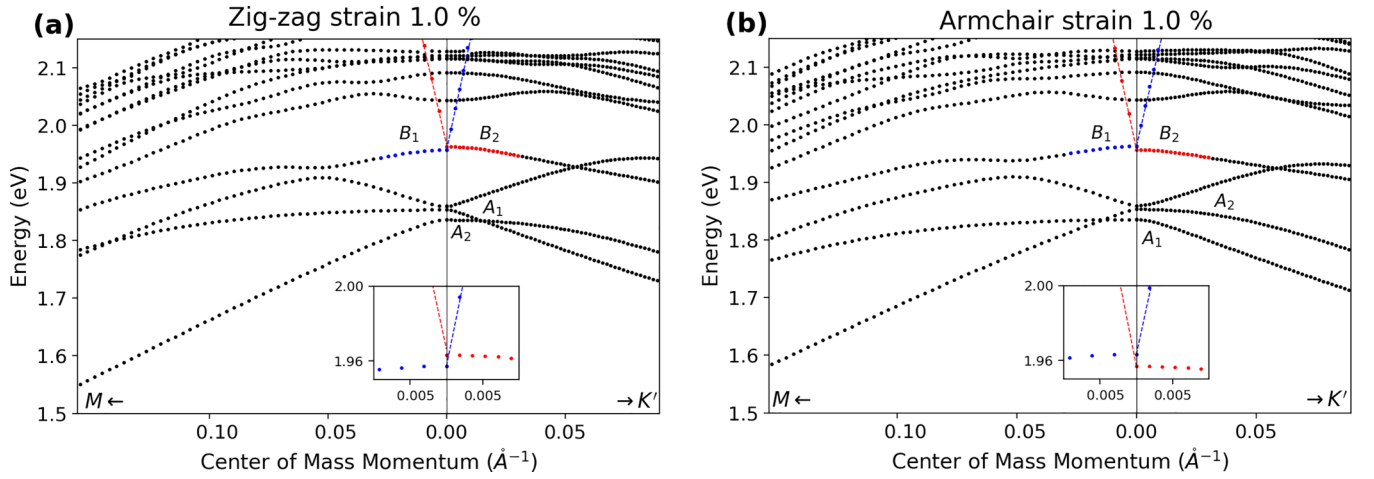


FIG. 13. Exciton dispersion in C_3N for \mathbf{Q} along the path $M\text{-}\Gamma\text{-}K'$, in the case of zigzag (a) and armchair strain (b). In both cases, the strain is fixed to 1.0%. The red (blue) dots denote the excitonic band dispersing from the B_2 (B_1) exciton at Γ . The insets show the excitonic branches departing from the bright excitons B_1 and B_2 at Γ . For completeness, $|\Gamma M| = 0.748 \text{ \AA}^{-1}$ and $|\Gamma K'| = 0.858 \text{ \AA}^{-1}$, in the case of zigzag strain, while $|\Gamma M| = 0.739 \text{ \AA}^{-1}$ and $|\Gamma K'| = 0.863 \text{ \AA}^{-1}$ in the case of armchair strain.

V-shaped dispersion, with the latter well reproduced by a linear dispersion with slope of about 19.0 eV \AA along both the ΓM and $\Gamma K'$ directions (see the dashed red line in Fig. 12). As discussed in the literature [38,46,49], this feature is due to the long-range component of the BSE exchange term, Eq. (7), in the excitonic Hamiltonian of 2D materials. In fact, this V-shaped dispersion combined with a slowly varying band is analogous to the dispersion discussed by Qiu *et al.* [46] for the excitonic bands departing from optically active twofold degenerate excitons in monolayer MoS_2 . A similar analysis is also proposed in the work of Cudazzo *et al.* in Ref. [38], and in a recent work by Qiu *et al.* (Ref. [49]).

We now turn our attention to the effect of uniaxial strain on the excitonic dispersion. In order to do this, we compute the excitonic dispersion at small \mathbf{Q} in the case of a strain equal to 1.0% applied along the zigzag and armchair directions. Similar considerations can also be done in the case of different strain values. The resulting dispersions are shown in Fig. 13. As previously discussed, the pair of bright excitons E_1 in pristine C_3N will split into B_1 and B_2 excitons. In the case of zigzag strain [Fig. 13(a)] the band originating from the lowest exciton B_1 is weakly dispersing along ΓM , while it has a linear trend along $\Gamma K'$ [see blue dots in Fig. 13(a)]. The situation is the opposite for the bands departing from the highest energy exciton B_2 , which is linear along ΓM and almost flat (with negative concavity) along the orthogonal direction $\Gamma K'$. These bands are highlighted by red dots in the figure. Similar consideration can be done for the bands originating from B_1 and B_2 in the case of armchair strain [see Fig. 13(b)].

The observed behavior is again due to the long-range component of the exchange kernel of the excitonic Hamiltonian. Qiu *et al.* [49] demonstrated that in 2D materials the excitonic dispersion of a band λ at small \mathbf{Q} can be written as

$$E_\lambda(\mathbf{Q}) = E_\lambda(\Gamma) + A_\lambda |\mathbf{Q}| \cos^2 \theta_{\mathbf{Q}} + \frac{\hbar^2 Q_x^2}{2M_\lambda^x} + \frac{\hbar^2 Q_y^2}{2M_\lambda^y}, \quad (19)$$

where $E_\lambda(\mathbf{Q} = \Gamma)$ is the energy of the nondegenerate exciton λ at null momentum and $\theta_{\mathbf{Q}}$ is the angle between \mathbf{D}_λ , defined

in Eq. (15), and the vector \mathbf{Q} . The terms showing a quadratic dependence on \mathbf{Q} are determined by the single-particle dispersions, the small- \mathbf{Q} behavior of the direct kernel, and the short-range part of the exchange kernel. These dependencies are captured by the exciton effective masses $M_\lambda^{x,y}$ which can be obtained by fitting *ab initio* results [46,49]. On the other hand, the linear term is only due to the long-range part of the exchange kernel, where A_λ is a coefficient proportional to the modulus of the exciton dipole \mathbf{D}_λ at $\mathbf{Q} = 0$.

Exploiting Eq. (19), we can give a rationale for the dispersions of the bands departing from the B_1 and B_2 excitons in strained C_3N . The exciton at Γ transforming as B_1 has a dipole \mathbf{D} with null component along the y direction, as it can only have OS for light polarization along x . Therefore, the band originating from this exciton (depicted in blue in Fig. 13) will have a linear dispersion along $\Gamma K'$, while it will be almost flat along ΓM . The reason is that if $\mathbf{Q} \parallel \Gamma M$, the cosine function $\cos^2 \theta_{\mathbf{Q}}$ is zero, so that the linear term in Eq. (19) does not contribute. Instead, the quadratic dispersion is due to the term proportional to Q_x^2 and Q_y^2 , with the negative concavity determined by the dependence on \mathbf{Q} of the difference $\epsilon_c(\mathbf{k} + \mathbf{Q}) - \epsilon_v(\mathbf{k})$. Conversely, the excitonic band originating from the exciton B_2 at Γ (highlighted by red dots in Fig. 13) will have a linear dispersion along ΓM and a quadratic one along $\Gamma K'$, as the dipole for B_2 excitons is oriented along the y direction parallel to ΓM , so that only if $\mathbf{Q} \parallel \Gamma M$ the linear term in Eq. (19) gives contribution, while if $\mathbf{Q} \parallel \Gamma K'$ this term is zero as the dipole is perpendicular to the exciton center-of-mass momentum.

We further point out that such a linear dispersion is only possible for exciton branches originating from bright excitons at Γ . The reason why the band starting from the third exciton (i.e., the one nondegenerate in pristine C_3N) does not show linear dispersion is a direct consequence of the small dipole strength acquired by this exciton under strain, so that the quadratic term dominates on the linear one in Eq. (19), even if the latter may be nonzero. As a last comment concerning the excitonic bands shown in Fig. 13, we remark that the two low-energy bands departing from the excitons A_1 and A_2 at Γ are

characterized by dispersions which are swapped passing from armchair to zigzag strain. The reason is strictly related to the fact that with zigzag strain the lowest exciton at Γ transforms as A_2 while the second exciton as A_1 . The order is reversed in the case of armchair strain, and, as a consequence, also the bands are exchanged. Finally, we can discuss our findings in view of the existing literature. In particular, our results concerning small- \mathbf{Q} exciton dispersion in strained C_3N highlight a peculiar effect related to exciton propagation in mechanically strained C_3N . In fact, Qiu *et al.* [49] pointed out that in 2D materials where optically bright excitons with strongly anisotropic dipole strength can exist (such as in single- or few-layer black phosphorous), it is possible to produce exciton wave packets which propagate along a quasi-1D channel, whose direction is defined by the orientation of the excitonic dipole at null momentum. This has been proved in the ballistic regime, and it has been demonstrated to be a consequence of the linearity of exciton bands at small momentum, for \mathbf{Q} parallel to the excitonic dipole.

Our results show that two bright excitons with intense oscillator strengths in orthogonal polarization directions are present in C_3N , at fixed uniaxial strain. As a consequence, in strained C_3N it should be possible to prepare exciton wave packets which propagate along either the armchair or the zigzag directions, according to the polarization of the incoming light beam which produce the wave packet itself. This is not possible for example in black phosphorous, as, in that case, the crystal does not have two excitons at Γ which are close in energy and characterized by orthogonal dipoles.

VII. CONCLUSIONS

In this work, we discuss in detail the effect of uniaxial strain on the excitonic properties of monolayer C_3N . First, we develop a simplified solution of the BSE based on a tight-binding description of single-particle properties (TB-BSE), coming from maximally localized Wannier functions obtained from the *ab initio* DFT calculations. This solution can also be applied to other 2D systems, with minor modifications. Such an approach allows us to investigate the effect of uniaxial strain on low-lying dark excitons and higher-energy active excitons in pristine C_3N . In particular, we discuss the origin of strain-induced optical anisotropy, as obtained from numerical calculations, in terms of group theory and symmetry arguments. Furthermore, we clarify the effect of strain on dark excitons, by demonstrating the strain-induced brightening of the lowest nondegenerate dark excitation. Such results could be exploited for device applications, such as optical switches, and we therefore hope that our study will stimulate optical spectroscopy experiments on C_3N under different strain configurations.

Finally, the developed TB-BSE approach allows us to obtain the excitonic dispersion in both pristine and strained C_3N , in a range of center-of-mass momenta \mathbf{Q} which are hardly accessible using state-of-the-art fully *ab initio* calculations. Our results on excitonic dispersions show that mechanically strained C_3N displays a peculiar selectivity effect in the propagation direction of the exciton wave packets along either the armchair or the zigzag paths. We therefore believe that the dynamics of excitons in strained C_3N should deserve

future experimental and theoretical investigation, in order to also clarify how other mechanisms affecting the exciton propagation (such as exciton-phonon coupling [50–53]) can be tuned by the applied mechanical strain.

ACKNOWLEDGMENTS

M.Z. thanks Fulvio Paleari, Alberto Guandalini, Savio Laricchia, and Marco Gibertini for illuminating discussions in the early stages of this project. The isosurfaces of MLWF have been displayed using the XCrySDen [54] program. The real-space exciton wave function has been shown using the PYBINDING package [55]. This work was partially funded by the EU through the MaX European Centre of Excellence: MaX (“MAterials design at the eXascale” [56]) funded by the European Union H2020-INFRAEDI-2018-1 programme, Grant No. 824143. It was also supported by the Italian national program PRIN2017 No. 2017BZPKSZ “Excitonic insulator in two-dimensional long-range interacting systems (EXC-INS).” Financial support from ICSCCentro Nazionale di Ricerca in High Performance Computing, Big Data and Quantum Computing, funded by European Union NextGenerationEU (Centro Nazionale 01 CN0000013 CUP B93C22000620006) is also acknowledged. A.R. acknowledges the project funded under the National Recovery and Resilience Plan (NRRP), Mission 04 Component 2 Investment 1.5 NextGenerationEU, Call for tender No. 3277, Award No. 0001052. M.J.C. acknowledges Brazilian agency CNPq and INEO (Natl. Inst. Sci. Technol. Organic Electronics - CNPq, FAPESP). Computational time on the Marconi100 machine at CINECA was provided by the Italian ISCRA program.

APPENDIX A: SYMMETRY OPERATIONS ON EXCITONS

In this section we discuss the method used within this work to assign an exciton λ to an irreducible representation of the planar point group of both pristine and strained ML- C_3N . Given an exciton λ , we assign it to the irreducible representation Γ if, given a symmetry operation \hat{S} of each class C of the group, we have that

$$\chi_C = \sum_{\lambda} \chi_S^{\lambda} = \sum_{\lambda} \int d\mathbf{r}_e d\mathbf{r}_h \Psi_{\lambda}^*(\mathbf{r}_e, \mathbf{r}_h) \hat{S} \Psi_{\lambda}(\mathbf{r}_e, \mathbf{r}_h) \quad (\text{A1})$$

is equal to the character of class C for the irreducible representation Γ . In Eq. (A1) the summation over λ is present only when we consider a manifold of degenerate excitons.

We now discuss how to compute the quantity χ_S^{λ} for a single exciton λ , also assuming that \hat{S} is a planar symmetry operator, which leaves unchanged the out-of-plane variable z . We start by writing the exciton wave function $\Psi_{\lambda}(\mathbf{r}_e, \mathbf{r}_h)$ in real space as

$$\Psi_{\lambda}(\mathbf{r}_e, \mathbf{r}_h) = \sum_{v\mathbf{c}\mathbf{k}} A_{\lambda}(v\mathbf{k}; c\mathbf{k}) \psi_{v\mathbf{k}}^*(\mathbf{r}_h) \psi_{c\mathbf{k}}(\mathbf{r}_e). \quad (\text{A2})$$

By defining

$$\psi_{\alpha\mathbf{k}}^W(\mathbf{r}) = \frac{1}{\sqrt{N}} \sum_{\mathbf{R}} e^{i\mathbf{k}\cdot\mathbf{R}} w(\mathbf{r} - \tau_{\alpha} - \mathbf{R}), \quad (\text{A3})$$

and writing the conduction and valence states c and v involved in the BSE in terms of the tight-binding coefficients $c_\alpha(n\mathbf{k})$, we can compactly write $\Psi_\lambda(\mathbf{r}_e, \mathbf{r}_h)$ as

$$\Psi_\lambda(\mathbf{r}_e, \mathbf{r}_h) = \sum_{\alpha\beta\mathbf{k}} \bar{A}_\lambda(\alpha\mathbf{k}; \beta\mathbf{k}) \psi_{\alpha\mathbf{k}}^{W*}(\mathbf{r}_h) \psi_{\beta\mathbf{k}}^W(\mathbf{r}_e), \quad (\text{A4})$$

where we have defined

$$\bar{A}_\lambda(\alpha\mathbf{k}; \beta\mathbf{k}) = \sum_{vc} A_\lambda(v\mathbf{k}; c\mathbf{k}) c_\alpha^*(v\mathbf{k}) c_\beta(c\mathbf{k}). \quad (\text{A5})$$

The action of the symmetry operator \hat{S} on a general \mathbf{r} -dependent function g is $\hat{S}g(\mathbf{r}) = g(\hat{S}^{-1}\mathbf{r})$, so, by straightforward generalization to two-variable functions, we have

$$\hat{S}\Psi_\lambda(\mathbf{r}_e, \mathbf{r}_h) = \Psi_\lambda(\hat{S}^{-1}\mathbf{r}_e, \hat{S}^{-1}\mathbf{r}_h)$$

and then χ_S^λ becomes

$$\chi_S^\lambda = \int d\mathbf{r}_e d\mathbf{r}_h \Psi_\lambda^*(\mathbf{r}_e, \mathbf{r}_h) \Psi_\lambda(\hat{S}^{-1}\mathbf{r}_e, \hat{S}^{-1}\mathbf{r}_h). \quad (\text{A6})$$

Using Eq. (A4) in Eq. (A6) we obtain

$$\begin{aligned} \chi_S^\lambda &= \sum_{\alpha_1\beta_1\mathbf{k}_1} \sum_{\alpha\beta\mathbf{k}} \bar{A}_\lambda^*(\alpha_1\mathbf{k}_1; \beta_1\mathbf{k}_1) \bar{A}_\lambda(\alpha\mathbf{k}; \beta\mathbf{k}) \\ &\quad \times I^e(\beta_1\mathbf{k}_1; \beta\mathbf{k}) I^h(\alpha_1\mathbf{k}_1; \alpha\mathbf{k}), \end{aligned} \quad (\text{A7})$$

where we have defined

$$\begin{aligned} I^e(\beta_1\mathbf{k}_1; \beta\mathbf{k}) &= \int d\mathbf{r}_e \psi_{\beta_1\mathbf{k}_1}^{W*}(\mathbf{r}_e) \psi_{\beta\mathbf{k}}^W(\hat{S}^{-1}\mathbf{r}_e), \\ I^h(\alpha_1\mathbf{k}_1; \alpha\mathbf{k}) &= \int d\mathbf{r}_h \psi_{\alpha_1\mathbf{k}_1}^W(\mathbf{r}_h) \psi_{\alpha\mathbf{k}}^{W*}(\hat{S}^{-1}\mathbf{r}_h). \end{aligned} \quad (\text{A8})$$

We now compute $I^e(\beta_1\mathbf{k}_1; \beta\mathbf{k})$ by using the definition of $\psi_{\beta\mathbf{k}}^W$, Eq. (A3), obtaining

$$\begin{aligned} I^e(\beta_1\mathbf{k}_1; \beta\mathbf{k}) &= \frac{1}{N} \sum_{\mathbf{R}\mathbf{R}_1} e^{-i\mathbf{k}_1 \cdot \mathbf{R}_1} e^{i\mathbf{k} \cdot \mathbf{R}} \int d\mathbf{r}_e \\ &\quad \times w(\mathbf{r}_e - \mathbf{R}_1 - \tau_{\beta_1}) w(\hat{S}^{-1}\mathbf{r}_e - \mathbf{R} - \tau_\beta). \end{aligned} \quad (\text{A9})$$

As the Wannier functions w used in this system have a $2p_z$ character, they transform according to

$$w(\hat{S}^{-1}\mathbf{r}_e - \mathbf{R} - \tau_{\beta_1}) = w(\mathbf{r}_e - \hat{S}\mathbf{R} - \hat{S}\tau_{\beta_1}) \quad (\text{A10})$$

if \hat{S} leaves unchanged the out-of-plane variable z . Defining the index β_S and the lattice vector \mathbf{R}_{β_S} such that $\hat{S}\tau_{\beta_1} = \mathbf{R}_{\beta_S} + \tau_{\beta_S}$, we find

$$\begin{aligned} &\int d\mathbf{r}_e w(\mathbf{r}_e - \mathbf{R}_1 - \tau_{\beta_1}) w(\hat{S}^{-1}\mathbf{r}_e - \mathbf{R} - \tau_\beta) \\ &= \delta_{\beta_1, \beta_S} \delta(\mathbf{R}_1 - \hat{S}\mathbf{R} - \mathbf{R}_{\beta_S}), \end{aligned} \quad (\text{A11})$$

where the orthonormality properties of MLWFs have been used. Therefore, by direct substitution in the definition of

$I^e(\beta_1\mathbf{k}_1; \beta\mathbf{k})$ and using the identity $\sum_{\mathbf{R}} e^{i\mathbf{k} \cdot \mathbf{R}} = N\delta_{\mathbf{k}, \mathbf{0}}$, valid for any \mathbf{k} vector in the BZ, we obtain

$$I^e(\beta_1\mathbf{k}_1; \beta\mathbf{k}) = \delta_{\beta_1, \beta_S} e^{-i\mathbf{k}_1 \cdot \mathbf{R}_{\beta_S}} \delta_{\mathbf{k}_1, \hat{S}\mathbf{k}}. \quad (\text{A12})$$

Proceeding in an analogous way we find

$$I^h(\alpha_1\mathbf{k}_1; \alpha\mathbf{k}) = \delta_{\alpha_1, \alpha_S} e^{i\mathbf{k}_1 \cdot \mathbf{R}_{\alpha_S}} \delta_{\mathbf{k}_1, \hat{S}\mathbf{k}}, \quad (\text{A13})$$

with α_S and \mathbf{R}_{α_S} such that $\hat{S}\tau_\alpha = \mathbf{R}_{\alpha_S} + \tau_{\alpha_S}$.

Finally, by substitution of Eqs. (A12) and (A13) in Eq. (A7) we obtain

$$\chi_S^\lambda = \sum_{\alpha\beta\mathbf{k}} \bar{A}_\lambda^*(\alpha_S\hat{S}\mathbf{k}; \beta_S\hat{S}\mathbf{k}) \bar{A}_\lambda(\alpha\mathbf{k}; \beta\mathbf{k}) e^{-i(\hat{S}\mathbf{k}) \cdot \mathbf{R}_{\beta_S}} e^{i(\hat{S}\mathbf{k}) \cdot \mathbf{R}_{\alpha_S}}. \quad (\text{A14})$$

We point out that Eq. (A14) gives meaningful results only if the coefficients c used to compute the \bar{A} functions are exactly the same used in the construction of the BSE kernel from which the envelope function $A_\lambda(v\mathbf{k}; c\mathbf{k})$ is obtained by diagonalization. If different coefficients are used, phase-inconsistency problems can arise.

APPENDIX B: EXCITON WAVE FUNCTIONS IN REAL SPACE

We define the real-space representation of exciton λ within our TB-BSE model as

$$\Psi_\lambda^{\alpha, \beta}(\mathbf{R}) = \langle \mathbf{r}_h = \tau_\alpha; \mathbf{r}_e = \tau_\beta + \mathbf{R} | \lambda \rangle, \quad (\text{B1})$$

where $|\mathbf{r}_h = \tau_\alpha; \mathbf{r}_e = \tau_\beta + \mathbf{R}\rangle$ is a compact notation to denote a 2-particle state, with an electron localized on the $2p_z$ -like orbital centered on atom β in the unit cell \mathbf{R} and a hole in the orbital localized on the atomic site α . Using Eq. (A4) for the exciton wave function in real space we obtain

$$\begin{aligned} \Psi_\lambda^{\alpha, \beta}(\mathbf{R}) &= \int d\mathbf{r}_e d\mathbf{r}_h w(\mathbf{r}_h - \tau_\alpha) w(\mathbf{r}_e - \mathbf{R} - \tau_\beta) \\ &\quad \times \sum_{\gamma\rho\mathbf{k}} \bar{A}(\gamma\mathbf{k}; \rho\mathbf{k}) \psi_{\gamma\mathbf{k}}^{W*}(\mathbf{r}_h) \psi_{\rho\mathbf{k}}^W(\mathbf{r}_e). \end{aligned} \quad (\text{B2})$$

A straightforward application of the orthogonality between MLWF localized on different atomic sites gives

$$\int d\mathbf{r}_h w(\mathbf{r}_h - \tau_\alpha) \psi_{\gamma\mathbf{k}}^{W*}(\mathbf{r}_h) = \frac{1}{\sqrt{N}} \delta_{\alpha, \gamma}, \quad (\text{B3})$$

$$\int d\mathbf{r}_e w(\mathbf{r}_e - \mathbf{R} - \tau_\beta) \psi_{\rho\mathbf{k}}^W(\mathbf{r}_e) = \frac{1}{\sqrt{N}} \delta_{\beta, \rho} e^{i\mathbf{k} \cdot \mathbf{R}}. \quad (\text{B4})$$

Finally, we obtain

$$\Psi_\lambda^{\alpha, \beta}(\mathbf{R}) = \frac{1}{N} \sum_{\mathbf{k}} e^{i\mathbf{k} \cdot \mathbf{R}} \bar{A}(\alpha\mathbf{k}; \beta\mathbf{k}). \quad (\text{B5})$$

[1] J. Mahmood, E. K. Lee, M. Jung, D. Shin, H.-J. Choi, J.-M. Seo, S.-M. Jung, D. Kim, F. Li, M. S. Lah, N.

Park, H.-J. Shin, J. H. Oh, and J.-B. Baek, Two-dimensional polyaniline (C₃N) from carbonized organic single crystals

- in solid state, *Proc. Natl. Acad. Sci. USA* **113**, 7414 (2016).
- [2] S. Yang, W. Li, C. Ye, G. Wang, H. Tian, C. Zhu, P. He, G. Ding, X. Xie, Y. Liu, Y. Lifshitz, S.-T. Lee, Z. Kang, and M. Jiang, C₃N—A 2D crystalline, hole-free, tunable-narrow-bandgap semiconductor with ferromagnetic properties, *Adv. Mater.* **29**, 1605625 (2017).
- [3] Y. Wu, W. Xia, W. Gao, F. Jia, P. Zhang, and W. Ren, Quasiparticle electronic structure of honeycomb C₃N: From monolayer to bulk, *2D Mater.* **6**, 015018 (2018).
- [4] Z. Tang, G. J. Cruz, Y. Wu, W. Xia, F. Jia, W. Zhang, and P. Zhang, Giant Narrow-Band Optical Absorption and Distinctive Excitonic Structures of Monolayer C₃N and C₃B, *Phys. Rev. Appl.* **17**, 034068 (2022).
- [5] M. Bonacci, M. Zanfognini, E. Molinari, A. Ruini, M. J. Caldas, A. Ferretti, and D. Varsano, Excitonic effects in graphene-like C₃N, *Phys. Rev. Mater.* **6**, 034009 (2022).
- [6] B. Mortazavi, Ultra high stiffness and thermal conductivity of graphene like C₃N, *Carbon* **118**, 25 (2017).
- [7] A. Bafekry, S. Farjami Shayesteh, and F. M. Peeters, C₃N monolayer: Exploring the emerging of novel electronic and magnetic properties with adatom adsorption, functionalizations, electric field, charging, and strain, *J. Phys. Chem. C* **123**, 12485 (2019).
- [8] L.-B. Shi, Y.-Y. Zhang, X.-M. Xiu, and H.-K. Dong, Structural characteristics and strain behavior of two-dimensional C₃N: First principles calculations, *Carbon* **134**, 103 (2018).
- [9] J. Xu, J. Mahmood, Y. Dou, S. Dou, F. Li, L. Dai, and J.-B. Baek, 2D frameworks of C₂N and C₃N as new anode materials for lithium-ion batteries, *Adv. Mater.* **29**, 1702007 (2017).
- [10] G.-C. Guo, R.-Z. Wang, B.-M. Ming, C. Wang, S.-W. Luo, M. Zhang, and H. Yan, C₃N/phosphorene heterostructure: A promising anode material in lithium-ion batteries, *J. Mater. Chem. A* **7**, 2106 (2019).
- [11] P. Bhauriyal, A. Mahata, and B. Pathak, Graphene-like carbon-nitride monolayer: A potential anode material for Na- and K-ion batteries, *J. Phys. Chem. C* **122**, 2481 (2018).
- [12] O. Faye, T. Hussain, A. Karton, and J. Szpunar, Tailoring the capability of carbon nitride (C₃N) nanosheets toward hydrogen storage upon light transition metal decoration, *Nanotechnology* **30**, 075404 (2019).
- [13] M. Makaremi, S. Grixti, K. T. Butler, G. A. Ozin, and C. V. Singh, Band engineering of carbon nitride monolayers by n-type, p-type, and isoelectronic doping for photocatalytic applications, *ACS Appl. Mater. Interfaces* **10**, 11143 (2018).
- [14] E. Blundo, M. Felici, T. Yildirim, G. Pettinari, D. Tedeschi, A. Miriametro, B. Liu, W. Ma, Y. Lu, and A. Polimeni, Evidence of the direct-to-indirect band gap transition in strained two-dimensional WS₂, MoS₂, and WSe₂, *Phys. Rev. Res.* **2**, 012024(R) (2020).
- [15] E. Blundo, A. Surrente, D. Spirito, G. Pettinari, T. Yildirim, C. A. Chavarin, L. Baldassarre, M. Felici, and A. Polimeni, Vibrational properties in highly strained hexagonal boron nitride bubbles, *Nano Lett.* **22**, 1525 (2022).
- [16] F. Carrascoso, R. Frisenda, and A. Castellanos-Gomez, Biaxial versus uniaxial strain tuning of single-layer MoS₂, *Nano Mater. Sci.* **4**, 44 (2022).
- [17] G. Strinati, Application of the Green's functions method to the study of the optical properties of semiconductors, *Riv. Nuovo Cim.* **11**, 1 (1988).
- [18] M. Rohlfing and S. G. Louie, Electron-hole excitations and optical spectra from first principles, *Phys. Rev. B* **62**, 4927 (2000).
- [19] G. Onida, L. Reining, and A. Rubio, Electronic excitations: Density-functional versus many-body Green's-function approaches, *Rev. Mod. Phys.* **74**, 601 (2002).
- [20] S. Latini, T. Olsen, and K. S. Thygesen, Excitons in van der Waals heterostructures: The important role of dielectric screening, *Phys. Rev. B* **92**, 245123 (2015).
- [21] F. Wu, F. Qu, and A. H. MacDonald, Exciton band structure of monolayer MoS₂, *Phys. Rev. B* **91**, 075310 (2015).
- [22] E. Ridolfi, C. H. Lewenkopf, and V. M. Pereira, Excitonic structure of the optical conductivity in MoS₂ monolayers, *Phys. Rev. B* **97**, 205409 (2018).
- [23] N. Marzari, A. A. Mostofi, J. R. Yates, I. Souza, and D. Vanderbilt, Maximally localized Wannier functions: Theory and applications, *Rev. Mod. Phys.* **84**, 1419 (2012).
- [24] J. P. Perdew, K. Burke, and M. Ernzerhof, Generalized Gradient Approximation Made Simple, *Phys. Rev. Lett.* **77**, 3865 (1996).
- [25] P. Giannozzi, S. Baroni, N. Bonini, M. Calandra, R. Car, C. Cavazzoni, D. Ceresoli, G. L. Chiarotti, M. Cococcioni, I. Dabo, A. D. Corso, S. de Gironcoli, S. Fabris, G. Fratesi, R. Gebauer, U. Gerstmann, C. Gougoussis, A. Kokalj, M. Lazzeri, L. Martin-Samos, *et al.*, Quantum ESPRESSO: A modular and open-source software project for quantum simulations of materials, *J. Phys.: Condens. Matter* **21**, 395502 (2009).
- [26] P. Giannozzi Jr., O. Andreussi, T. Brumme, O. Bunau, M. B. Nardelli, M. Calandra, R. Car, C. Cavazzoni, D. Ceresoli, M. Cococcioni, N. Colonna, I. Carnimeo, A. D. Corso, S. de Gironcoli, P. Delugas, R. A. DiStasio, A. Ferretti, A. Floris, G. Fratesi, G. Fugallo, *et al.*, Advanced capabilities for materials modelling with Quantum ESPRESSO, *J. Phys.: Condens. Matter* **29**, 465901 (2017).
- [27] N. Marzari and D. Vanderbilt, Maximally localized generalized Wannier functions for composite energy bands, *Phys. Rev. B* **56**, 12847 (1997).
- [28] A. A. Mostofi, J. R. Yates, Y.-S. Lee, I. Souza, D. Vanderbilt, and N. Marzari, wannier90: A tool for obtaining maximally-localised Wannier functions, *Comput. Phys. Commun.* **178**, 685 (2008).
- [29] A. A. Mostofi, J. R. Yates, G. Pizzi, Y.-S. Lee, I. Souza, D. Vanderbilt, and N. Marzari, An updated version of wannier90: A tool for obtaining maximally-localised Wannier functions, *Comput. Phys. Commun.* **185**, 2309 (2014).
- [30] G. Pizzi, V. Vitale, R. Arita, S. Blgel, F. Freimuth, G. Géranton, M. Gibertini, D. Gresch, C. Johnson, T. Koretsune, J. Ibañez-Azpiroz, H. Lee, J.-M. Lihm, D. Marchand, A. Marrazzo, Y. Mokrousov, J. I. Mustafa, Y. Nohara, Y. Nomura, L. Paulatto, S. Poncé, *et al.*, Wannier90 as a community code: New features and applications, *J. Phys.: Condens. Matter* **32**, 165902 (2020).
- [31] I. Souza, N. Marzari, and D. Vanderbilt, Maximally localized Wannier functions for entangled energy bands, *Phys. Rev. B* **65**, 035109 (2001).
- [32] See Supplemental Material at <http://link.aps.org/supplemental/10.1103/PhysRevB.107.045430> for details on the *ab initio* calculations, and for the derivations of the BSE correlation and exchange kernels within the TB description of single-particle properties.

- [33] P. Lechiffart, F. Paleari and C. Attaccalite, Excitons under strain: Light absorption and emission in strained hexagonal boron nitride, *SciPost Phys.* **12**, 145 (2022).
- [34] C. A. Rozzi, D. Varsano, A. Marini, E. K. U. Gross, and A. Rubio, Exact Coulomb cutoff technique for supercell calculations, *Phys. Rev. B* **73**, 205119 (2006).
- [35] D. A. Hamann, Optimized norm-conserving Vanderbilt pseudopotentials, *Phys. Rev. B* **88**, 085117 (2013).
- [36] P. Cudazzo, I. V. Tokatly, and A. Rubio, Dielectric screening in two-dimensional insulators: Implications for excitonic and impurity states in graphane, *Phys. Rev. B* **84**, 085406 (2011).
- [37] H. J. Monkhorst and J. D. Pack, Special points for Brillouin-zone integrations, *Phys. Rev. B* **13**, 5188 (1976).
- [38] P. Cudazzo, L. Sponza, C. Giorgetti, L. Reining, F. Sottile, and M. Gatti, Exciton Band Structure in Two-Dimensional Materials, *Phys. Rev. Lett.* **116**, 066803 (2016).
- [39] A. Marini, C. Hogan, M. Grüning, and D. Varsano, yambo: An *ab initio* tool for excited state calculations, *Comput. Phys. Commun.* **180**, 1392 (2009).
- [40] D. Sangalli, A. Ferretti, H. Miranda, C. Attaccalite, I. Marri, E. Cannuccia, P. Melo, M. Marsili, F. Paleari, A. Marrazzo, G. Prandini, P. Bonfà, M. O. Atambo, F. Affinito, M. Palummo, A. Molina-Sánchez, C. Hogan, M. Grüning, D. Varsano, and A. Marini, Many-body perturbation theory calculations using the yambo code, *J. Phys.: Condens. Matter* **31**, 325902 (2019).
- [41] K. Andersen, S. Latini, and K. S. Thygesen, Dielectric genome of van der Waals heterostructures, *Nano Lett.* **15**, 4616 (2015).
- [42] Q.-Y. Chen, M.-y. Liu, C. Cao, and Y. He, Anisotropic optical properties induced by uniaxial strain of monolayer C₃N: A first-principles study, *RSC Adv.* **9**, 13133 (2019).
- [43] T. Galvani, F. Paleari, H. P. C. Miranda, A. Molina-Sánchez, L. Wirtz, S. Latil, H. Amara, and F. Ducastelle, Excitons in boron nitride single layer, *Phys. Rev. B* **94**, 125303 (2016).
- [44] M. Dresselhaus, *Group Theory: Application to the Physics of Condensed Matter* (Springer, Berlin, 2008).
- [45] M. Gatti and F. Sottile, Exciton dispersion from first principles, *Phys. Rev. B* **88**, 155113 (2013).
- [46] D. Y. Qiu, T. Cao, and S. G. Louie, Nonanalyticity, Valley Quantum Phases, and Lightlike Exciton Dispersion in Monolayer Transition Metal Dichalcogenides: Theory and First-Principles Calculations, *Phys. Rev. Lett.* **115**, 176801 (2015).
- [47] M. Palummo, M. Bernardi, and J. C. Grossman, Exciton radiative lifetimes in two-dimensional transition metal dichalcogenides, *Nano Lett.* **15**, 2794 (2015).
- [48] H.-Y. Chen, V. A. Jhalani, M. Palummo, and M. Bernardi, *Ab initio* calculations of exciton radiative lifetimes in bulk crystals, nanostructures, and molecules, *Phys. Rev. B* **100**, 075135 (2019).
- [49] D. Y. Qiu, G. Cohen, D. Novichkova, and S. Refaely-Abramson, Signatures of dimensionality and symmetry in exciton band structure: Consequences for exciton dynamics and transport, *Nano Lett.* **21**, 7644 (2021).
- [50] P. Cudazzo, First-principles description of the exciton-phonon interaction: A cumulant approach, *Phys. Rev. B* **102**, 045136 (2020).
- [51] F. Paleari and A. Marini, Exciton-phonon interaction calls for a revision of the exciton concept, *Phys. Rev. B* **106**, 125403 (2022).
- [52] G. Antonius and S. G. Louie, Theory of exciton-phonon coupling, *Phys. Rev. B* **105**, 085111 (2022).
- [53] H.-Y. Chen, D. Sangalli, and M. Bernardi, Exciton-Phonon Interaction and Relaxation Times from First Principles, *Phys. Rev. Lett.* **125**, 107401 (2020).
- [54] A. Kokalj, XCrySDen: A new program for displaying crystalline structures and electron densities, *J. Mol. Graphics Modell.* **17**, 176 (1999).
- [55] D. Moldovan, M. Anđelković, and F. Peeters, pybinding v0.9.5: A Python package for tight-binding calculations, Zenodo 826942, 2020.
- [56] www.max-centre.eu.